CrossMark

J. Fluid Mech. (2015), *vol.* 770, *pp.* 5–26. © Cambridge University Press 2015
doi:10.1017/jfm.2015.129

Driven particles at fluid interfaces acting as capillary dipoles

Aaron Dörr[1,†] **and Steffen Hardt**[1]

[1]Institute for Nano- and Microfluidics, Center of Smart Interfaces, Technische Universität Darmstadt, Alarich-Weiss-Straße 10, 64287 Darmstadt, Germany

(Received 23 September 2014; revised 9 January 2015; accepted 23 February 2015; first published online 30 March 2015)

The dynamics of spherical particles driven along an interface between two immiscible fluids is investigated asymptotically. Under the assumptions of a pinned three-phase contact line (TCL) and very different viscosities of the two fluids, a particle assumes a tilted orientation. As it moves, it causes a deformation of the fluid interface which is also computed. The case of two interacting driven particles is studied via the linear superposition approximation. It is shown that the capillary interaction force resulting from the particle motion is dipolar in terms of the azimuthal angle and decays with the fifth power of the inter-particle separation, similar to a capillary quadrupole originating from undulations of the TCL. The dipolar interaction is demonstrated to exceed the quadrupolar interaction at moderate particle velocities.

Key words: capillary flows, contact lines, low-Reynolds-number flows

1. Introduction

Macroscopic phenomena involving particles attached to the interface between two immiscible fluids offer a wide variety of interesting fields of research (e.g. Kralchevsky & Nagayama 2000; Ghezzi *et al.* 2001; Binks 2002; Horozov, Aveyard & Clint 2005; Koser, Keim & Arratia 2013). In contrast to bulk suspensions (Russel, Saville & Schowalter 1989), both the fluid interface itself as well as the difference in the properties of the two fluids, on the one hand, influence the forces acting on individual particles, and, on the other hand, introduce additional mechanisms for particle–particle interactions.

Regarding individual particles, researchers have studied the particles' equilibrium configuration at the fluid interface (Nicolson 1949; Huh & Mason 1974; Singh & Hesla 2004), their temporal response to external disturbances (Singh *et al.* 2011), the work necessary to detach particles from a fluid interface (Pitois & Chateau 2002), their interfacial mobility under external forcing (Fulford & Blake 1986; O'Neill, Ranger & Brenner 1986; Danov *et al.* 1995; Petkov *et al.* 1995; Danov *et al.* 1998; Cichocki *et al.* 2004; Fischer, Dhar & Heinig 2006; Pozrikidis 2007; Ally & Amirfazli 2010; Bławzdziewicz, Ekiel-Jeżewska & Wajnryb 2010) as well as the related diffusion coefficient (Radoev, Nedjalkov & Djakovich 1992; Chen & Tong 2008; Du, Liddle & Berglund 2012; Sriram, Walder & Schwartz 2012). Unexpected behaviour in the

†Email address for correspondence: doerr@csi.tu-darmstadt.de

https://doi.org/10.1017/jfm.2015.129 Published online by Cambridge University Press

diffusion coefficient has been observed (Chen & Tong 2008; Sriram *et al.* 2012) and attributed to possible configurational changes in the system, e.g. detachment of particles from the fluid interface.

Particle–particle interactions arising from deformations of the fluid–fluid interface due to external forces and/or irregular menisci have been studied extensively (Nicolson 1949; Chan, Henry & White 1981; Fortes 1982; Kralchevsky & Nagayama 2000; Stamou, Duschl & Johannsmann 2000; Ghezzi *et al.* 2001; Binks 2002; Danov *et al.* 2005; Oettel, Domínguez & Dietrich 2005; Singh & Joseph 2005; Vassileva *et al.* 2005; Domínguez, Oettel & Dietrich 2008; Oettel & Dietrich 2008). In particular, Singh & Joseph (2005) and Vassileva *et al.* (2005) have discussed hydrodynamic interactions of interfacial particles approaching each other, the latter reference containing direct numerical simulations of interacting floating particles. Concerning capillary interactions at large separations, a modelling approach is the linear superposition approximation or LSA, introduced by Nicolson (1949) and occasionally used within later studies (e.g. Chan *et al.* 1981; Oettel *et al.* 2005; Vassileva *et al.* 2005). The LSA exploits knowledge of the fluid–fluid interfacial deformation around a single particle by approximating the two-particle deformation via linear superposition of two single-particle deformations.

As already mentioned, a number of studies have dealt with single driven particles at fluid–fluid interfaces. Those studies may be divided into two groups. The first group assume that the fluid–fluid interface is either planar (O'Neill *et al.* 1986; Danov *et al.* 1995; Cichocki *et al.* 2004; Fischer *et al.* 2006; Ally & Amirfazli 2010; Bławzdziewicz *et al.* 2010; Würger 2014) or has a given shape (Petkov *et al.* 1995) unaffected by the particle motion, thus focusing on a purely hydrodynamic problem and aiming at the mobility tensor of the particle. Some of the publications from the first group consider interfacial incompressibility or viscosity, properties originating from the presence of surfactants or associated with membranes, as opposed to pure interfaces. The second group investigate the deformation of a fluid interface caused by a moving particle. This group also includes works on particles moving parallel to the fluid interface without touching the latter (Lee, Chadwick & Leal 1979; Berdan & Leal 1982). In all of these studies, the interfacial shape approximated either asymptotically (Lee *et al.* 1979; Berdan & Leal 1982; Radoev *et al.* 1992), numerically (Fulford & Blake 1986; Pozrikidis 2007), or based on a combined approach (Danov *et al.* 1998), shows maximum deviation from the planar interface on the axis of the particle motion and zero deviation along the axis perpendicular to it, corresponding to a dipolar deformation.

Remarkably, among the studies on driven particles, only the methods of Pozrikidis (2007) and, in the context of floating particles, Singh & Joseph (2005) require the specification of a boundary condition for the fluid–fluid interfacial shape at the particle surface. In both cases, a constant contact angle is specified. By contrast, when a particle moves along an interface with a pinned three-phase contact line (TCL), which is a physically reasonable assumption for relatively small particle velocities, the contact angle varies along the TCL as a result of hydrodynamic forces acting on the fluid interface. Therefore, we use the assumptions of a pinned TCL and a varying contact angle throughout the present paper. The effect of a limited range of contact angle hysteresis will be discussed further below.

As an additional motivation for the present study, we consider a particle driven by an external force acting on the particle's centre of mass and parallel to the fluid interface. As the particle moves subject to the force, it approaches a steady-state velocity until finally the drag force balances the external force. However, when there

https://doi.org/10.1017/jfm.2015.129 Published online by Cambridge University Press

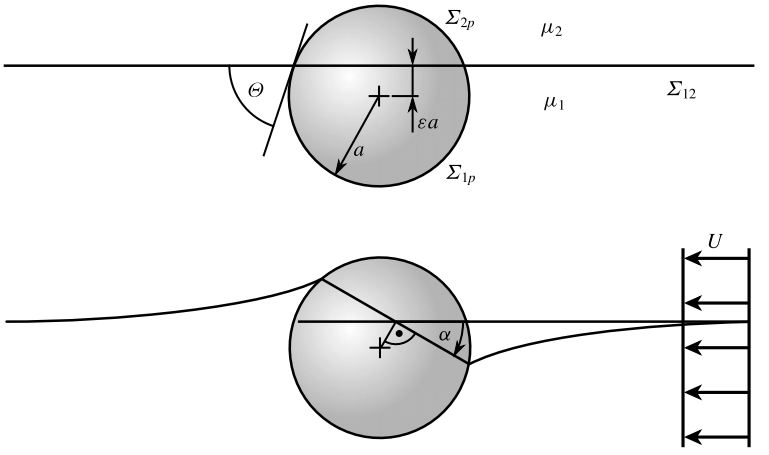


FIGURE 1. Sketch of a spherical particle p attached to the interface Σ_{12} between fluids 1 and 2. (*a*) Equilibrium configuration in the absence of any external force with static contact angle Θ. (*b*) Steady-state configuration of the driven particle moving with a constant velocity of U according to the case $\mu_1 > \mu_2$, viewed in the particle's rest frame. The particle is rotated by the trim angle α.

exists a viscosity difference between the two fluids, the drag force's line of action generally does not run through the particle's centre of mass. Therefore, the drag force is accompanied by a torque on the particle. As a consequence, the particle is rotated until the hydrodynamic torque is balanced by the torque due to interfacial tension. Thus, the initial particle configuration is not sustained because it is inconsistent with the balance of angular momentum. To the best of our knowledge, the effect just described has not been studied before in the context of interfacial particles and will be the main topic of the present work. As a side remark, a similar configurational change is known from ship hydrodynamics (Rawson 2001). In that context, the configuration is quantified in terms of the so-called trim angle. We adopt that notation for the present paper.

In the following, we describe the interplay between hydrodynamic and interfacial tension forces by means of an asymptotic model. The flow field is calculated as a first step and then utilized to approximate the interfacial shape. In the last step, the angular momentum balance for the particle yields the particle trim angle. Once the final configuration of the one-particle system is known, the LSA enables us to discuss the resulting dipolar particle–particle interactions. Finally, we comment on possible consequences and extensions of the model.

2. Modelling approach

We consider a rigid spherical particle of radius a attached to the interface Σ_{12} between two immiscible fluids 1 and 2, as depicted in figure 1. The circular TCL is pinned to the particle surface $\Sigma_{1p} \cup \Sigma_{2p}$. Since the particle radius is the characteristic length scale of the flow field, we may neglect undulations of the TCL, which are typically tens of nanometres in size (Stamou *et al.* 2000; Park & Furst 2011), when dealing with microparticles. For simplicity, we assume the Bond number $Bo := \Delta\rho g a^2/\sigma_{12}$, containing the maximum density difference $\Delta\rho$ between the three phases, the gravitational acceleration g as well as the fluid–fluid interfacial tension

https://doi.org/10.1017/jfm.2015.129 Published online by Cambridge University Press

σ_{12}, to be zero. The assumption $Bo = 0$ leads to the equilibrium configuration shown in figure 1(*a*), characterized by a planar interface and an equilibrium contact angle Θ. Note that there is no conceptual difficulty in including a non-zero Bond number within the asymptotic model described below, since Lee *et al.* (1979) have demonstrated that the perturbation quantity may be a combination of the Bond number and the capillary number $Ca := \mu_1 U/\sigma_{12}$ used in the present work. In the definition of Ca, μ_1 denotes the dynamic viscosity of fluid 1, while U denotes the absolute value of the undisturbed flow velocity far from the particle when the situation is analysed in the particle's rest frame (see figure 1*b*). The force $\boldsymbol{F}$ driving the particle is supposed to act at the particle's centre of mass and parallel to the plane given by the fluid interface in equilibrium. As discussed above, the plane containing the circular TCL has rotated by the trim angle α once the particle motion has reached a steady state (see figure 1*b*). In the regime of particle Reynolds numbers $Re := Ua/\nu_1$ much smaller than unity, where ν_1 denotes the kinematic viscosity of fluid 1, incompressible Newtonian fluid flow is governed by the Stokes equation

$$\boldsymbol{0} = -\boldsymbol{\nabla} p + \mu \boldsymbol{\nabla}^2 \boldsymbol{u} \tag{2.1}$$

and the continuity equation

$$\boldsymbol{\nabla} \cdot \boldsymbol{u} = 0, \tag{2.2}$$

where $\boldsymbol{u}$ is the velocity and p is the pressure. In (2.1) and (2.2), indices 1 and 2 denoting the respective fluid phases have been omitted. On the particle surface, the flow field obeys the no-slip condition

$$\boldsymbol{u} = \boldsymbol{0} \quad \text{at} \quad \Sigma_{1p} \cup \Sigma_{2p} \tag{2.3}$$

while approaching the homogeneous velocity field $\boldsymbol{U}$ far from the particle. Across the fluid–fluid interface, which is assumed pure and therefore non-viscous (zero Boussinesq number), implying absence of Marangoni stresses, the velocity is continuous,

$$[\![\boldsymbol{u}]\!] = \boldsymbol{0} \quad \Longleftrightarrow \quad \boldsymbol{u}_1 = \boldsymbol{u}_2 \quad \text{at} \quad \Sigma_{12}, \tag{2.4}$$

and we have the interfacial momentum balance equation

$$[\![-p\boldsymbol{I} + 2\mu \boldsymbol{S}]\!] \cdot \boldsymbol{n}_{12} = \sigma_{12} \left(\boldsymbol{\nabla}^s \cdot \boldsymbol{n}_{12}\right) \boldsymbol{n}_{12} \quad \text{at} \quad \Sigma_{12}, \tag{2.5}$$

where $\boldsymbol{I}$ and $\boldsymbol{S}$ are the unit tensor and the rate-of-strain tensor, respectively, $\boldsymbol{n}_{12}$ is the fluid interface normal, and $\boldsymbol{\nabla}^s := (\boldsymbol{I} - \boldsymbol{n}_{12} \otimes \boldsymbol{n}_{12}) \cdot \boldsymbol{\nabla}$. In (2.4) and (2.5), we have used the jump bracket notation

$$[\![f]\!](\boldsymbol{r}) := \left[f(\boldsymbol{r} + \epsilon \boldsymbol{n}_{12}) - f(\boldsymbol{r} - \epsilon \boldsymbol{n}_{12})\right]_{\epsilon \to 0} = f_1(\boldsymbol{r}) - f_2(\boldsymbol{r}) \quad \text{for } \boldsymbol{r} \in \Sigma_{12}. \tag{2.6}$$

Note that the last part of (2.6) implies that the orientation of the normal vector with respect to the fluid phases has been specified in such a way that it points from fluid 2 into fluid 1. Concerning the particle having the outer normal vector $\boldsymbol{n}_p$, steady state is reached when the balances of linear momentum

$$\boldsymbol{0} = \iint_{\Sigma_{1p} \cup \Sigma_{2p}} \boldsymbol{T} \cdot \boldsymbol{n}_p \mathrm{d}\Sigma + \oint_{TCL} \sigma_{12} \left(\frac{\partial \boldsymbol{r}_{TCL}}{\partial s} \times \boldsymbol{n}_{12} \right) \mathrm{d}s + \boldsymbol{F} \tag{2.7}$$

https://doi.org/10.1017/jfm.2015.129 Published online by Cambridge University Press

and angular momentum with respect to the particle's centre of mass

$$\mathbf{0} = \iint_{\Sigma_{1p}\cup\Sigma_{2p}} \boldsymbol{r}_p \times (\boldsymbol{T}\cdot\boldsymbol{n}_p)\mathrm{d}\Sigma + \oint_{TCL} \boldsymbol{r}_{TCL} \times \left[\sigma_{12}\left(\frac{\partial \boldsymbol{r}_{TCL}}{\partial s}\times \boldsymbol{n}_{12}\right)\right]\mathrm{d}s \tag{2.8}$$

are fulfilled. Note that the inertial contributions to the balances (2.7) and (2.8) have been neglected since the Reynolds number is much smaller than unity. In (2.7) and (2.8), $\boldsymbol{T} := -p\boldsymbol{I} + 2\mu\boldsymbol{S}$ is the stress tensor, $\boldsymbol{r}_{TCL}$ is the position vector of a point on the TCL, parametrized by s such that the vector $\partial\boldsymbol{r}_{TCL}/\partial s \times \boldsymbol{n}_{12}$ points away from the particle, and $\boldsymbol{r}_p$ is the position vector of a point on the particle surface. Recall that by definition the driving force $\boldsymbol{F}$ itself does not produce a torque on the particle as it acts on its centre of mass. We concentrate on the case of a low viscosity ratio between the two fluids, implying $\mu_2/\mu_1 \to 0$, because in that case the effects studied in this work are expected to be most pronounced, and also because explicit analytical results can be found. Upon introducing the scaling

$$\boldsymbol{u} =: U\tilde{\boldsymbol{u}} \quad p =: \frac{\tilde{p}\mu_1 U}{a} \quad \boldsymbol{S} =: \frac{\tilde{\boldsymbol{S}}U}{a} \quad \nabla =: \frac{1}{a}\tilde{\nabla} \tag{2.9a–d}$$

and incorporating the definition of the jump bracket (2.6) and of the capillary number Ca, we may write the interfacial momentum balance (2.5) as

$$-\tilde{p}_1\boldsymbol{n}_{12} + 2\tilde{\boldsymbol{S}}_1\cdot\boldsymbol{n}_{12} = Ca^{-1}(\tilde{\nabla}^s\cdot\boldsymbol{n}_{12})\boldsymbol{n}_{12}, \tag{2.10}$$

where the stress contribution due to fluid 2 is omitted according to the assumption of low viscosity ratio, $\mu_2/\mu_1 \to 0$. The presence of the factor Ca^{-1} on the right-hand side of (2.10) allows for a perturbation approach in which zeroth-order stresses cause a first-order deformation of the fluid interface, and correspondingly for higher orders. In the present work, we focus on the first-order deformation. An extension to higher orders is formally straightforward, but is not expected to yield much additional insight. For any quantity f, the perturbation series for small capillary numbers is given by

$$f =: f^{(0)} + f^{(1)}Ca + O(Ca^2). \tag{2.11}$$

Accordingly, the interfacial stress balance (2.10) becomes

$$\left(-\tilde{p}_1^{(0)}\boldsymbol{n}_{12}^{(0)} + 2\tilde{\boldsymbol{S}}_1^{(0)}\cdot\boldsymbol{n}_{12}^{(0)}\right)Ca = \left(\tilde{\nabla}^s\cdot\boldsymbol{n}_{12}^{(1)}\right)\boldsymbol{n}_{12}^{(0)}Ca + O(Ca^2), \tag{2.12}$$

where the planarity of the zeroth-order fluid interface, $\tilde{\nabla}^s\cdot\boldsymbol{n}_{12}^{(0)} = 0$, has been used.

3. Flow field and stress distribution

As we are interested in the first-order curvature of the fluid interface represented by $\tilde{\nabla}^s\cdot\boldsymbol{n}_{12}^{(1)}$, it is obvious from (2.12) that the flow field of order $Ca^{(0)}$ is to be described. Physically, the case $Ca = 0$ implies that the interfacial tension is large enough to counterbalance any jump in the normal stresses across the fluid interface without noticeable interfacial deformation. Moreover, because of the low viscosity ratio assumption, the stress vector at the fluid–fluid interface is perpendicular to the latter, similar to a symmetry boundary. The flow scenario within the half-space occupied by fluid 1 at $Ca = 0$ and $\mu_2/\mu_1 = 0$ can thus be imitated by notionally

https://doi.org/10.1017/jfm.2015.129 Published online by Cambridge University Press

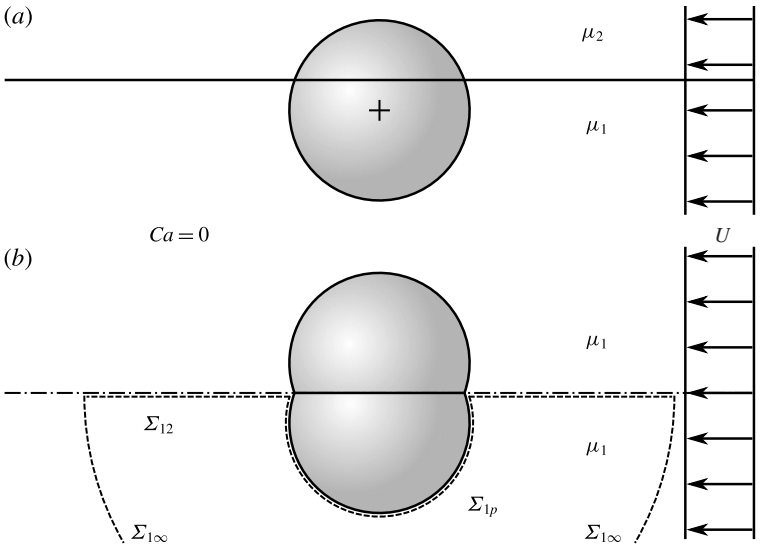


FIGURE 2. Equivalent problems for describing the flow field within fluid 1 at zero capillary number and zero viscosity ratio. (*a*) Original scenario including the planar fluid–fluid interface and the spherical particle. (*b*) Transformed scenario with symmetry plane (dash-dotted) and two fused equal spheres; the control volume (dashed) utilized in the calculation of the torque is also shown.

removing the fluid interface and replacing fluid 2 by fluid 1. At the same time, the part of the rigid particle originally wetted by fluid 1 must be mirrored with respect to the planar fluid interface, making the latter a symmetry plane for the flow problem. Figure 2 provides a sketch of the two setups which are equivalent with respect to the flow of fluid 1. The procedure just described allows for a convenient treatment of the flow problem based on Stokes flow around a body moving parallel to its symmetry plane (usually termed asymmetric flow as opposed to axisymmetric flow). In the case of a spherical particle with an equilibrium contact angle Θ (see figure 1*a*) of 90°, the flow field of order Ca^0 is given by the well-known Stokes flow problem past a sphere (Happel & Brenner 1983).

Figure 3 defines the spherical coordinate system used in the subsequent asymptotic analysis of the flow field. Herein, the x-axis points downwards into the region originally occupied by fluid 1. The depicted configuration corresponds to $\varepsilon > 0$ and therefore $\Theta < 90°$, as shown in figure 1(*a*). Clearly, we have the relation

$$\varepsilon = \cos\Theta. \tag{3.1}$$

The undisturbed fluid infinitely remote from the particle flows into the negative z direction when U is positive, that is $\boldsymbol{U} = -U\boldsymbol{e}_z$. A formal solution to the Stokes flow problem around two fused spheres with arbitrary ε was developed by Zabarankin (2007). However, that solution is not suited to the present work since we intend to derive explicit analytical expressions capturing the main effects, while evaluating the results by Zabarankin (2007) requires the solution of a Fredholm integral equation. Therefore, we choose an asymptotic approach developed by Brenner (1964) (see also Happel & Brenner 1983). The method is based on a representation of the particle shape (in our case, the fused spheres) as a power series in a geometric perturbation

https://doi.org/10.1017/jfm.2015.129 Published online by Cambridge University Press

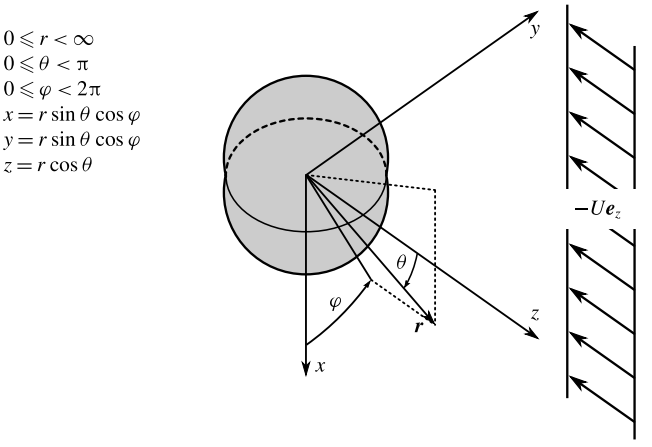


FIGURE 3. Spherical coordinates and the direction of the undisturbed flow at infinity.

quantity (in our case, ε) by means of surface spherical harmonics. In this way, the no-slip boundary condition (2.3) on the generally non-spherical particle surface may be approximated by a more complicated velocity boundary condition on a spherical particle surface. Upon fitting the general solution of the Stokes equation (2.1), as given by Lamb (1932), in terms of solid spherical harmonics, to the boundary condition projected onto the spherical surface written in terms of surface spherical harmonics, the specific solution to the flow problem can be determined. Such an asymptotic approach implies that we focus on a situation in which the contact angle Θ is not too far from 90°.

Consulting figures 3 and 1(*a*), we see that the coordinates of a point $\boldsymbol{r}_p = r_p \boldsymbol{e}_r = x_p \boldsymbol{e}_x + y_p \boldsymbol{e}_y + z_p \boldsymbol{e}_z$ on the particle–fluid interface obey the relation

$$(x_p - \varepsilon a)^2 + y_p^2 + z_p^2 = a^2 \tag{3.2}$$

in the Cartesian system, and consequently

$$\tilde{r}_p = \varepsilon \sin\theta \, |\cos\varphi| + \sqrt{\varepsilon^2 \left(\sin^2\theta \cos^2\varphi - 1\right) + 1} \sim 1 + \varepsilon \sin\theta \, |\cos\varphi| \tag{3.3}$$

in spherical coordinates and non-dimensional quantities. Within the scope of the present work, it is sufficient to restrict the analysis to first order in ε. Additionally, in order to simplify notation, we usually omit higher-order terms in ε, keeping in mind that the subsequent expressions containing ε are valid only up to first order. The particle shape is therefore approximately given by

$$\tilde{r}_p = 1 + \varepsilon \sin\theta \, |\cos\varphi| \, . \tag{3.4}$$

According to the method by Brenner (1964), we need to expand the last term in (3.4) into a series of surface spherical harmonics,

$$\sin\theta \, |\cos\varphi| = \sum_{k=0}^{\infty} f_k(\theta, \varphi), \tag{3.5}$$

https://doi.org/10.1017/jfm.2015.129 Published online by Cambridge University Press

		c_{km}			c_{km}
$k=0$	$m=0$	$\sqrt{\pi}$	$k=8$	$m=0$	$-35\sqrt{17\pi}/16\,384$
$k=2$	$m=0$	$-\sqrt{5\pi}/8$		$m=2$	$3\sqrt{595\pi/2}/4096$
	$m=2$	$\sqrt{15\pi}/8$		$m=4$	$-3\sqrt{1309\pi}/8192$
$k=4$	$m=0$	$-3\sqrt{\pi}/64$		$m=6$	$\sqrt{7293\pi/2}/4096$
	$m=2$	$\sqrt{5\pi}/32$		$m=8$	$-3\sqrt{12\,155\pi}/16\,384$
	$m=4$	$-\sqrt{35\pi}/64$	$k=10$	$m=0$	$-147\sqrt{21\pi}/131\,072$
$k=6$	$m=0$	$-5\sqrt{13\pi}/1024$		$m=2$	$49\sqrt{385\pi}/131\,072$
	$m=2$	$\sqrt{1365\pi/2}/1024$		$m=4$	$-7\sqrt{5005\pi}/65\,536$
	$m=4$	$-3\sqrt{91\pi}/1024$		$m=6$	$21\sqrt{5005\pi/2}/131\,072$
	$m=6$	$\sqrt{3003\pi/2}/1024$		$m=8$	$-7\sqrt{85\,085\pi/3}/131\,072$
				$m=10$	$7\sqrt{323\,323\pi/6}/131\,072$

TABLE 1. Expansion coefficients c_{km} for two fused spheres approximated to first order in ε as calculated from (3.9); coefficients with $m<0$ and/or m odd vanish.

where f_k is a surface spherical harmonic of order k defined by

$$\nabla^2\left(r^k f_k\right)=0. \tag{3.6}$$

In more detail, using the associated Legendre polynomials $P_k^m(\cos\theta)$, we write (Byerly 1893; Dassios & Vafeas 2001)

$$f_k(\theta,\varphi)=\sum_{m=0}^{k} c_{km}N_{km}P_k^m(\cos\theta)\cos(m\varphi) \tag{3.7}$$

with the normalization coefficients

$$N_{km}=\begin{cases}\sqrt{2}\sqrt{\dfrac{2k+1}{4\pi}\dfrac{(k-m)!}{(k+m)!}} & \text{if } m>0,\\[2ex] \sqrt{\dfrac{2k+1}{4\pi}} & \text{if } m=0.\end{cases} \tag{3.8}$$

The expansion coefficients c_{km} are given by

$$c_{km}=\int_0^{\pi}\int_0^{2\pi}\sin\theta\,|\cos\varphi|\,N_{km}P_k^m(\cos\theta)\cos(m\varphi)\sin\theta\,\mathrm{d}\theta\,\mathrm{d}\varphi. \tag{3.9}$$

We have omitted the terms corresponding to $m<0$, associated with $\sin(m\varphi)$, in (3.7) and (3.8) since the respective c_{km} can be shown to vanish in the expansion (3.5). In table 1, the first few expansion coefficients are listed. Now that we know the spherical harmonics expansion of the $O(\varepsilon)$-approximation of two fused spheres, we turn to the calculation of the solution

$$\tilde{\boldsymbol{u}}^{(0)}=:\tilde{\boldsymbol{u}}^{(0,0)}+\varepsilon\tilde{\boldsymbol{u}}^{(0,1)}+O(\varepsilon^2) \tag{3.10}$$

https://doi.org/10.1017/jfm.2015.129 Published online by Cambridge University Press

and analogously for the pressure $\tilde{p}^{(0)}$. Recalling that $\varepsilon = 0$ describes the case of a particle with a contact angle of 90° (or, equivalently, two fused spheres collapsed into a single sphere), it is obvious that

$$\tilde{\boldsymbol{u}}^{(0,0)} = -\frac{1}{2}\cos\theta\left(\frac{1}{\tilde{r}^3} - \frac{3}{\tilde{r}} + 2\right)\boldsymbol{e}_r - \frac{1}{4}\sin\theta\left(\frac{1}{\tilde{r}^3} + \frac{3}{\tilde{r}} - 4\right)\boldsymbol{e}_\theta, \tag{3.11}$$

$$\tilde{p}^{(0,0)} = \frac{3}{2}\frac{\cos\theta}{\tilde{r}^2}, \tag{3.12}$$

which is the solution to the classical problem of Stokes flow past a sphere (Happel & Brenner 1983). Regarding the $O(\varepsilon)$-term in (3.10), Brenner (1964) has constructed the boundary condition

$$\tilde{\boldsymbol{u}}^{(0,1)}\Big|_{\tilde{r}=1} = -\sin\theta|\cos\phi|\left.\frac{\partial\tilde{\boldsymbol{u}}^{(0,0)}}{\partial\tilde{r}}\right|_{\tilde{r}=1} = -\sum_{k=0}^{\infty} f_k(\theta,\varphi)\left.\frac{\partial\tilde{\boldsymbol{u}}^{(0,0)}}{\partial\tilde{r}}\right|_{\tilde{r}=1} \tag{3.13}$$

projected onto a single sphere. The formalism leading to the velocity and pressure fields $\tilde{\boldsymbol{u}}^{(0,1)}$ and $\tilde{p}^{(0,0)}$ can be found elsewhere (Brenner 1964; Happel & Brenner 1983). However, although that method can in principle be directly applied to the problem of fused spheres, corrections to certain formulae given in the above references are needed. If the formalism is applied consistently with Brenner (1964) and Happel & Brenner (1983), the results for the velocity and pressure fields do not solve the Stokes equation. For the special case $\boldsymbol{U} = -U\boldsymbol{e}_z$ discussed here, we will thus provide the corrected expressions using the same notation as Brenner (1964). To be precise, equations (3.22) and (3.23) given by Brenner (1964) need to be reformulated. The goal is to express the right-hand side of

$$\sum_{n=1}^{\infty} {}_kY_n^{(1)} = \frac{3}{2}\left(\tilde{r}\tilde{\boldsymbol{U}}\cdot\tilde{\boldsymbol{\nabla}}f_k - 2f_k\tilde{\boldsymbol{U}}\cdot\boldsymbol{e}_r\right) \tag{3.14}$$

through a sum of surface spherical harmonics to find the ${}_kY_n^{(1)}$. Since $\tilde{\boldsymbol{U}} = -\boldsymbol{e}_z$ in the present work, after some calculation we arrive at

$$\begin{aligned}\sum_{n=1}^{\infty} {}_kY_n^{(1)} \;=\; -\frac{3}{2}\sum_{m=0}^{k}\frac{c_{km}N_{km}\cos(m\varphi)}{2k+1}\big[&(1-k)(k+m)P_{k-1}^m(\cos\theta)\\ &+(2+k)(k-m+1)P_{k+1}^m(\cos\theta)\big],\end{aligned} \tag{3.15}$$

replacing equation (3.22) by Brenner (1964) and allowing us to read off

$${}_kY_n^{(1)} = \begin{cases} \dfrac{3}{2}\displaystyle\sum_{m=0}^{k}\frac{c_{km}N_{km}\cos(m\varphi)}{2k+1}(k-1)(k+m)P_{k-1}^m(\cos\theta) & \text{for } n=k-1,\\ -\dfrac{3}{2}\displaystyle\sum_{m=0}^{k}\frac{c_{km}N_{km}\cos(m\varphi)}{2k+1}(2+k)(k-m+1)P_{k+1}^m(\cos\theta) & \text{for } n=k+1,\\ 0 & \text{for all other } n. \end{cases} \tag{3.16}$$

https://doi.org/10.1017/jfm.2015.129 Published online by Cambridge University Press

In conjunction with equations (2.12*a–c*) by Brenner (1964) and Lamb's solution (Brenner 1964, equations (2.13*a*,*b*)), (3.16) yields the expressions for $\tilde{\boldsymbol{u}}^{(0,1)}$ and $\tilde{p}^{(0,1)}$. As those expressions are very lengthy, we waive writing them down at this point and go over to deriving the force and torque acting on the particle as well as the stress at the fluid–fluid interface. Due to the symmetry, the drag force $\boldsymbol{F}_D^{(0)}$ on the particle in figure 2(*a*) is simply half the drag force on the mirrored particle in figure 2(*b*). The latter can be calculated based on equation (2.20) by Brenner (1964), which is well-suited to the perturbation approach used above, and is found to be

$$\boldsymbol{F}_D^{(0)} = -3\pi\mu_1 Ua\left(1+\tfrac{9}{16}\varepsilon\right)\boldsymbol{e}_z. \tag{3.17}$$

As expected, if $\varepsilon = 0$, the drag is half the Stokes drag of a sphere (Radoev *et al.* 1992; Danov *et al.* 1995; Ally & Amirfazli 2010). Equally intuitive is the increase in drag with increasing ε, that is, deeper immersion of the particle in fluid 1. We now turn to the torque acting on the particle, occurring in the balance of angular momentum (2.8) and therefore required to determine the trim angle α. Instead of directly calculating the torque on the particle, we write down the y-component of the balance of angular momentum for the control volume enclosed by the interfaces Σ_{12}, Σ_{1p} and $\Sigma_{1\infty}$ shown in figure 2(*b*), which reads

$$\begin{aligned} 0 \;=\; \boldsymbol{e}_y \cdot \Bigg[&\iint_{\Sigma_{12}} \boldsymbol{r}\times(\boldsymbol{T}^{(0)}\cdot\boldsymbol{n}^{(0)})\mathrm{d}\Sigma + \iint_{\Sigma_{1p}} \boldsymbol{r}\times(\boldsymbol{T}^{(0)}\cdot\boldsymbol{n}^{(0)})\mathrm{d}\Sigma \\ &+ \iint_{\Sigma_{1\infty}} \boldsymbol{r}\times(\boldsymbol{T}^{(0)}\cdot\boldsymbol{n}^{(0)})\mathrm{d}\Sigma \Bigg], \end{aligned} \tag{3.18}$$

where the vectors $\boldsymbol{n}^{(0)}$ are outer normals with respect to the control volume. Again, inertial terms have been neglected according to the assumption of small Reynolds numbers. The second integral on the right-hand side of (3.18) is equal to the negative of the viscous torque acting on the particle (from (2.8)) in the case $\mu_2/\mu_1 = 0$. The third integral can be shown to vanish as the radius of the hemispherical interface $\Sigma_{1\infty}$ goes to infinity. We therefore only need to calculate the integral over the fluid–fluid interface Σ_{12} whose integrand contains the stress distribution on Σ_{12} (which is equal to the stress difference across the interface when $\mu_2/\mu_1 = 0$). Conveniently, the same stress distribution is required for the calculation of the $O(Ca)$ interfacial deformation further below. We have already noted that the fluid–fluid interface of order Ca^0 is a symmetry boundary to which the stress vector is perpendicular. Since for $Ca = 0$ we see from figure 3 that the outer normal at Σ_{12} is $\boldsymbol{e}_\varphi$ at $\varphi = \pi/2$ and $-\boldsymbol{e}_\varphi$ at $\varphi = 3\pi/2$, only the component $T_{\varphi\varphi}^{(0)}$ is non-zero. The latter is given by

$$\begin{aligned} \tilde{T}_{\varphi\varphi}^{(0)} \;=\; \sum_{\nu=1}^{\infty} \frac{\tau_\nu^{(0)}}{\tilde{r}^{2\nu+2}}\cos\theta = \Bigg[&-\left(\frac{3}{2}+\frac{33}{8}\varepsilon\right)\frac{1}{\tilde{r}^4} + \frac{1485}{512}\frac{\varepsilon}{\tilde{r}^6} + \frac{105}{128}\frac{\varepsilon}{\tilde{r}^8} + \frac{28\,035}{65\,536}\frac{\varepsilon}{\tilde{r}^{10}} \\ &+ \frac{35\,343}{131\,072}\frac{\varepsilon}{\tilde{r}^{12}} + \frac{3144\,141}{1677\,216}\frac{\varepsilon}{\tilde{r}^{14}} + \frac{2323\,035}{16\,777\,216}\frac{\varepsilon}{\tilde{r}^{16}} \\ &+ \frac{485\,474\,445}{4294\,967\,296}\frac{\varepsilon}{\tilde{r}^{18}} + \frac{729\,555\,255}{8589\,934\,592}\frac{\varepsilon}{\tilde{r}^{20}} + \cdots \Bigg]\cos\theta \end{aligned} \tag{3.19}$$

at both $\varphi = \pi/2$ and $\varphi = 3\pi/2$. Remarkably, the stress distribution has the form of an infinite series in negative powers of $\tilde{r}$. As a consequence, we need to check the

https://doi.org/10.1017/jfm.2015.129 Published online by Cambridge University Press

convergence of any quantity dependent on $\tilde{T}^{(0)}_{\varphi\varphi}$. Now we are in a position to evaluate

$$\begin{aligned}
&\boldsymbol{e}_y \cdot \iint_{\Sigma_{12}} \boldsymbol{r} \times (\boldsymbol{T}^{(0)} \cdot \boldsymbol{n}^{(0)}) \mathrm{d}\Sigma \\
&\quad = 2 \int_{a\sqrt{1-\varepsilon^2}}^{\infty} \int_0^{\pi} \boldsymbol{e}_y \cdot \left[r\boldsymbol{e}_r \times \left(\boldsymbol{T}^{(0)} \cdot \boldsymbol{e}_\varphi \right) \right]_{\varphi=\pi/2} r \mathrm{d}\theta \mathrm{d}r && (3.20) \\
&\quad = 2 \int_{a}^{\infty} \int_0^{\pi} \boldsymbol{e}_y \cdot \left[r\boldsymbol{e}_r \times \left(\boldsymbol{T}^{(0)} \cdot \boldsymbol{e}_\varphi \right) \right]_{\varphi=\pi/2} r \mathrm{d}\theta \mathrm{d}r + O(\varepsilon^2) && (3.21) \\
&\quad = 2 \int_{a}^{\infty} \int_0^{\pi} \boldsymbol{e}_y \cdot \left[r\boldsymbol{e}_r \times \left(T^{(0)}_{\varphi\varphi} \boldsymbol{e}_\varphi \right) \right]_{\varphi=\pi/2} r \mathrm{d}\theta \mathrm{d}r + O(\varepsilon^2) && (3.22) \\
&\quad = -2\mu_1 U a^2 \int_1^{\infty} \int_0^{\pi} \tilde{T}^{(0)}_{\varphi\varphi}\Big|_{\varphi=\pi/2} \tilde{r}^2 \cos\theta \mathrm{d}\theta \mathrm{d}\tilde{r} \ \text{(to order } \varepsilon) && (3.23) \\
&\quad \overset{(3.19)}{=} \pi\mu_1 U a^2 \sum_{\nu=1}^{\infty} \frac{\tau^{(0)}_\nu}{2\nu - 1}, && (3.24)
\end{aligned}$$

which will be used further below for finding the trim angle α.

4. Interfacial deformation and particle trim angle

In order to parametrize the shape of the fluid–fluid interface Σ_{12} of order Ca – resulting, within the perturbation approach, from the stress distribution of order Ca^0 calculated above – we introduce circular cylindrical coordinates $(\varrho, \vartheta, \chi)$,

$$\varrho = r|_{x=0}\,, \quad \vartheta = 2\pi - \theta, \quad \text{and} \quad \chi = x = r\sin\theta\cos\varphi, \tag{4.1a–c}$$

allowing us to utilize the expression (3.19) for the stress distribution by setting $\tilde{r} \to \tilde{\varrho}$ and $\theta \to 2\pi - \vartheta$. Note that in the cylindrical coordinate system $0 \leqslant \vartheta < 2\pi$, in contrast to $0 \leqslant \theta < \pi$ for spherical coordinates, which does not introduce a sign error but helps us to avoid the distinction between the regions of positive and negative y (that is, between $\varphi = \pi/2$ and $\varphi = 3\pi/2$ at $x = 0$) necessary in the context of spherical coordinates (cf. (4.6) below). Within the cylindrical coordinate system, we measure the interfacial deformation through its undulation in the direction of the χ-axis,

$$\boldsymbol{r}_{12} = \varrho\boldsymbol{e}_\varrho + h(\varrho, \vartheta)\boldsymbol{e}_\chi. \tag{4.2}$$

By choosing the orientation of the normal vector $\boldsymbol{n}_{12}$ consistently with the jump condition (2.5), we obtain

$$\boldsymbol{n}_{12} = \frac{\dfrac{\partial \boldsymbol{r}_{12}}{\partial\varrho} \times \dfrac{\partial \boldsymbol{r}_{12}}{\partial\vartheta}}{\left\| \dfrac{\partial \boldsymbol{r}_{12}}{\partial\varrho} \times \dfrac{\partial \boldsymbol{r}_{12}}{\partial\vartheta} \right\|} = \frac{-\dfrac{\partial h}{\partial\varrho}\boldsymbol{e}_\varrho - \dfrac{1}{\varrho}\dfrac{\partial h}{\partial\vartheta}\boldsymbol{e}_\vartheta + \boldsymbol{e}_\chi}{\sqrt{1 + \left(\dfrac{\partial h}{\partial\varrho}\right)^2 + \left(\dfrac{1}{\varrho}\dfrac{\partial h}{\partial\vartheta}\right)^2}} \tag{4.3}$$

and insert the expansion $h = h^{(1)}Ca + O(Ca^2)$. We are led to

$$\boldsymbol{n}_{12} = \boldsymbol{n}^{(0)}_{12} + \boldsymbol{n}^{(1)}_{12} Ca + O(Ca^2) = \boldsymbol{e}_\chi - \left(\frac{\partial h^{(1)}}{\partial\varrho}\boldsymbol{e}_\varrho + \frac{1}{\varrho}\frac{\partial h^{(1)}}{\partial\vartheta}\boldsymbol{e}_\vartheta \right) Ca + O(Ca^2) \tag{4.4}$$

https://doi.org/10.1017/jfm.2015.129 Published online by Cambridge University Press

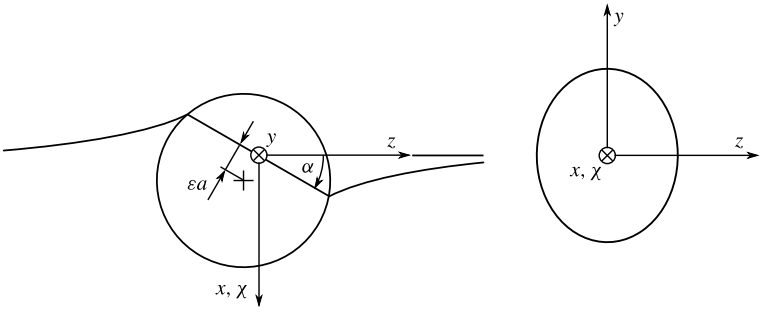


FIGURE 4. Geometry of the TCL when both α and ε are positive.

as well as to the curvature

$$\nabla^s \cdot \boldsymbol{n}_{12} = -\left(\frac{\partial^2 h^{(1)}}{\partial \varrho^2} + \frac{1}{\varrho}\frac{\partial h^{(1)}}{\partial \varrho} + \frac{1}{\varrho^2}\frac{\partial^2 h^{(1)}}{\partial \vartheta^2}\right) Ca + O(Ca^2). \tag{4.5}$$

In order to evaluate the interfacial momentum balance (2.12), we need to specify the sign of the stress deforming the interface. Since the left-hand side of (2.12) is equal to the term $\tilde{\boldsymbol{T}}^{(0)} \cdot \boldsymbol{n}_{12}^{(0)}$ and we are interested in the normal component of the stress, we may write (using $\boldsymbol{n}_{12}^{(0)} = \boldsymbol{e}_\chi = \boldsymbol{e}_x$ according to (4.4))

$$\left(\tilde{\boldsymbol{T}}^{(0)} \cdot \boldsymbol{n}_{12}^{(0)}\right) \cdot \boldsymbol{n}_{12}^{(0)} = \begin{cases} \left(-\tilde{\boldsymbol{T}}^{(0)} \cdot \boldsymbol{e}_\varphi\right) \cdot (-\boldsymbol{e}_\varphi) = \tilde{T}_{\varphi\varphi}^{(0)} & \text{for } \varphi = \pi/2, \\ \left(\tilde{\boldsymbol{T}}^{(0)} \cdot \boldsymbol{e}_\varphi\right) \cdot \boldsymbol{e}_\varphi = \tilde{T}_{\varphi\varphi}^{(0)} & \text{for } \varphi = 3\pi/2. \end{cases} \tag{4.6}$$

Insertion of (4.5), (4.6), and (3.19) – now in cylindrical coordinates – into the jump condition (2.12) and scalar multiplication with $\boldsymbol{n}_{12}^{(0)}$ yields

$$-\sum_{\nu=1}^{\infty} \frac{\tau_\nu^{(0)}}{\tilde{\varrho}^{2\nu+2}} \cos\vartheta = \frac{\partial^2 \tilde{h}^{(1)}}{\partial \tilde{\varrho}^2} + \frac{1}{\tilde{\varrho}}\frac{\partial \tilde{h}^{(1)}}{\partial \tilde{\varrho}} + \frac{1}{\tilde{\varrho}^2}\frac{\partial^2 \tilde{h}^{(1)}}{\partial \vartheta^2}. \tag{4.7}$$

In addition, boundary conditions for h are to be specified. At $\varrho \to \infty$, obviously we have $h \to 0$ because the origin of the cylindrical coordinate system coincides with the centre of the disk enclosed by the TCL (see figure 4). A closer look is needed concerning the boundary condition on the TCL which has an elliptic shape with principal axes $2a\sqrt{1-\varepsilon^2}$ and $2a\sqrt{1-\varepsilon^2}\cos\alpha$ when projected onto the yz-plane. The coordinates of a point $\boldsymbol{r}_{TCL}$ on the TCL can be found by first describing a circle of radius $a\sqrt{1-\varepsilon^2}$ embedded in the yz-plane and, secondly, by rotating the coordinate system by an angle of α around the y-axis. One obtains

$$\boldsymbol{r}_{TCL} = a\sqrt{\frac{1-\varepsilon^2}{\sin^2\vartheta\cos^2\alpha + \cos^2\vartheta}}(\cos\alpha\boldsymbol{e}_\varrho + \cos\vartheta\sin\alpha\boldsymbol{e}_\chi). \tag{4.8}$$

Since the trim angle α depends on the particle velocity, it can be written as $\alpha = \alpha^{(1)}Ca + O(Ca^2)$. In conjunction with $\sqrt{1-\varepsilon^2} = 1 + O(\varepsilon^2)$ and by omission of the terms $O(\varepsilon^2)$, (4.8) is simplified to

$$\tilde{\boldsymbol{r}}_{TCL} = \boldsymbol{e}_\varrho + \alpha^{(1)}\cos\vartheta Ca\,\boldsymbol{e}_\chi + O(Ca^2). \tag{4.9}$$

https://doi.org/10.1017/jfm.2015.129 Published online by Cambridge University Press

Considering the parametrization (4.2) and expanding

$$\tilde{h}^{(1)}|_{TCL} = \tilde{h}^{(1)}(1, \vartheta) + O(Ca), \tag{4.10}$$

we read off the boundary condition

$$\tilde{h}^{(1)}(1, \vartheta) = \alpha^{(1)} \cos\vartheta. \tag{4.11}$$

It is now straightforward to find the solution to (4.7) consistent with the boundary conditions (4.11) and $\tilde{h}^{(1)}(\tilde{\varrho} \to \infty, \vartheta) = 0$, which is given by

$$\tilde{h}^{(1)}(\tilde{\varrho}, \vartheta) = \left[\frac{\alpha^{(1)}}{\tilde{\varrho}} + \sum_{\nu=1}^{\infty} \frac{\tau_\nu^{(0)}}{1-4\nu^2} \left(\frac{1}{\tilde{\varrho}^{2\nu}} - \frac{1}{\tilde{\varrho}} \right) \right] \cos\vartheta. \tag{4.12}$$

Note that the trim angle $\alpha^{(1)}$ is still unknown and is to be determined from the angular momentum balance (2.8). Owing to the identical stress term $\partial \boldsymbol{r}_{TCL}/\partial s \times \boldsymbol{n}_{12}$ in (2.7) and (2.8), we can derive the expression for $\boldsymbol{F}$ in parallel to the one for $\alpha^{(1)}$. The parametrization is chosen as $\mathrm{d}\tilde{s} = \mathrm{d}\vartheta$ (recall that the stress vector will be oriented outwards with respect to the particle). Since $\partial \boldsymbol{e}_\varrho/\partial\vartheta = \boldsymbol{e}_\vartheta$, we may deduce from (4.9)

$$\frac{\partial \tilde{\boldsymbol{r}}_{TCL}}{\partial \tilde{s}} = \frac{\partial \tilde{\boldsymbol{r}}_{TCL}}{\partial \vartheta} = \boldsymbol{e}_\vartheta - \alpha^{(1)} \sin\vartheta \boldsymbol{e}_\chi Ca + O(Ca^2). \tag{4.13}$$

The fluid–fluid interfacial normal vector $\boldsymbol{n}_{12}$, or – as a consequence of (4.4) – the derivatives of $\tilde{h}^{(1)}$ with respect to $\tilde{\varrho}$ and ϑ, need to be evaluated at the TCL. Analogously to (4.10), this means that the derivatives of $\tilde{h}^{(1)}$ in (4.4) are to be evaluated at $(1, \vartheta)$ as long as we limit the analysis to first order in Ca. As a result, we find

$$\frac{\partial \tilde{\boldsymbol{r}}_{TCL}}{\partial \tilde{s}} \times \boldsymbol{n}_{12} = \boldsymbol{e}_\varrho + Ca \left. \frac{\partial \tilde{h}^{(1)}}{\partial \tilde{\varrho}} \right|_{(1,\vartheta)} \overset{(4.12)}{=} \boldsymbol{e}_\varrho - Ca \left(\alpha^{(1)} - \sum_{\nu=1}^{\infty} \frac{\tau_\nu^{(0)}}{1+2\nu} \right) \cos\theta \boldsymbol{e}_\chi. \tag{4.14}$$

Obviously, the integral along the TCL occurring in (2.7) vanishes, which implies that interfacial tension does not contribute to the drag. The driving force $\boldsymbol{F}^{(0)}$ is therefore equal to the negative of the drag force $\boldsymbol{F}_D^{(0)}$. In the case of the y-component of (2.8), normalized by $\sigma_{12}a^2$, a similar calculation using the result (4.14) yields

$$\boldsymbol{e}_y \cdot \oint_{TCL} \tilde{\boldsymbol{r}}_{TCL} \times \left(\frac{\partial \tilde{\boldsymbol{r}}_{TCL}}{\partial \tilde{s}} \times \boldsymbol{n}_{12} \right) \mathrm{d}\tilde{s} = -\pi Ca \left(2\alpha^{(1)} - \sum_{\nu=1}^{\infty} \frac{\tau_\nu^{(0)}}{1+2\nu} \right). \tag{4.15}$$

As has been discussed above in the context of (3.18), the viscous torque acting on the particle is equal to the negative of the viscous torque (3.24) acting on the fluid volume enclosed by the interfaces Σ_{12}, Σ_{1p} and $\Sigma_{1\infty}$ (recall figure 2*b*):

$$\boldsymbol{e}_y \cdot \iint_{\Sigma_{1p} \cup \Sigma_{2p}} \tilde{\boldsymbol{r}}_p \times (\tilde{\boldsymbol{T}}^{(0)} \cdot \boldsymbol{n}_p) \mathrm{d}\tilde{\Sigma} = -\boldsymbol{e}_y \cdot \iint_{\Sigma_{12}} \tilde{\boldsymbol{r}} \times (\tilde{\boldsymbol{T}}^{(0)} \cdot \boldsymbol{n}^{(0)}) \mathrm{d}\tilde{\Sigma} = \pi Ca \sum_{\nu=1}^{\infty} \frac{\tau_\nu^{(0)}}{1-2\nu}. \tag{4.16}$$

https://doi.org/10.1017/jfm.2015.129 Published online by Cambridge University Press

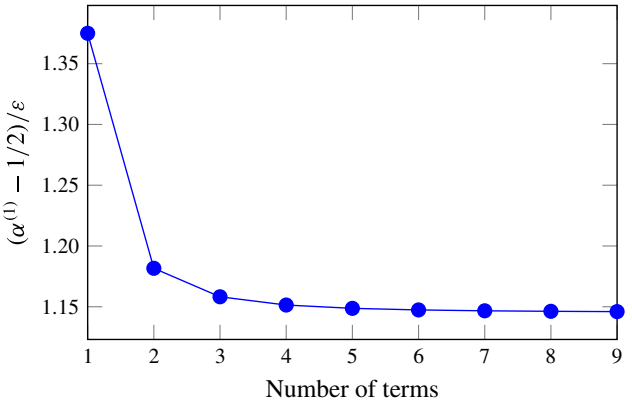


FIGURE 5. (Colour online) Convergence plot for the $O(\varepsilon)$-term in (4.17).

The y-component of (2.8) can now be solved by insertion of the expressions (4.15) and (4.16). We are led to the result for the particle trim angle to first order in Ca,

$$\alpha = \sum_{\nu=1}^{\infty} \frac{\tau_\nu^{(0)}}{1-4\nu^2} Ca + O(Ca^2) \approx \left(\frac{1}{2} + 1.146\varepsilon\right) Ca + O(Ca^2), \tag{4.17}$$

where the numerical value of 1.146 corresponds to the sum of the first nine terms. The convergence of expression (4.17) is demonstrated in figure 5. By means of the result for $\alpha^{(1)}$ we can write down the final formula describing the interfacial shape,

$$\tilde{h}^{(1)}(\tilde{\varrho}, \vartheta) = \sum_{\nu=1}^{\infty} \frac{\tau_\nu^{(0)}}{(1-4\nu^2)\tilde{\varrho}^{2\nu}} \cos\vartheta, \tag{4.18}$$

which is visualized in figure 6 for a capillary number of $Ca = 0.3$ and an equilibrium contact angle of $\Theta = 75°$. The lower half-space is occupied by fluid 1 and the particle is moving to the right of the picture. A white line piercing through the north and south poles of the sphere has been added to indicate the change in orientation, that is, the trim angle. From figure 6 it can be seen that the contact angle changes around the particle's circumference. While the contact angle retains its equilibrium value at $\vartheta = \pi/2$ and $3\pi/2$, it deviates most strongly from that value at $\vartheta = 0$ and π. From geometric considerations (see also figure 4), the deviation at $\vartheta = 0$ is found to be

$$\delta\Theta = \sum_{\nu=1}^{\infty} \frac{\tau_\nu^{(0)}}{1-2\nu} Ca + O(Ca^2) \approx \left(\frac{3}{2} + 2.863\varepsilon\right) Ca + O(Ca^2), \tag{4.19}$$

where again nine terms have been included in the summation. At $\vartheta = \pi$, the contact angle difference $\delta\Theta$ has the same magnitude but the opposite sign. Figure 7 shows cross-sections of the interfacial shape and the TCL in the plane $\tilde{y} = 0$ for three different contact angles Θ. The particle trim angle, indicated by the inclination of the TCL plane between $\tilde{z} = -1$ and $\tilde{z} = 1$, obviously increases when the particle plunges deeper into fluid 1 (larger ε) with its relatively high viscosity, which is an intuitive result.

https://doi.org/10.1017/jfm.2015.129 Published online by Cambridge University Press

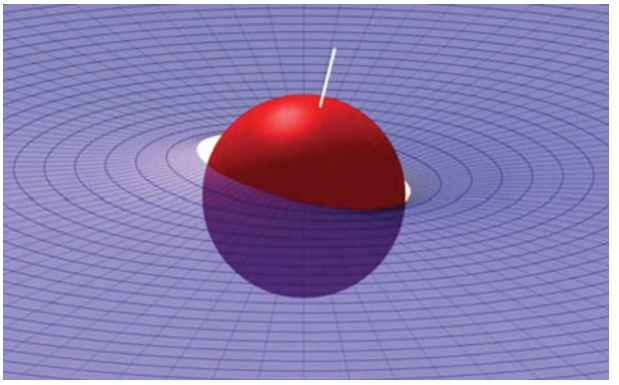


FIGURE 6. (Colour online) Visualization of the $O(Ca^1)$-configuration for an equilibrium contact angle Θ of 75° and a capillary number of $Ca = 0.3$. The trim angle can be estimated from the inclination of the white line. The gap between the particle surface and the fluid–fluid interface arises because the boundary condition is evaluated on a cylindrical surface according to (4.10).

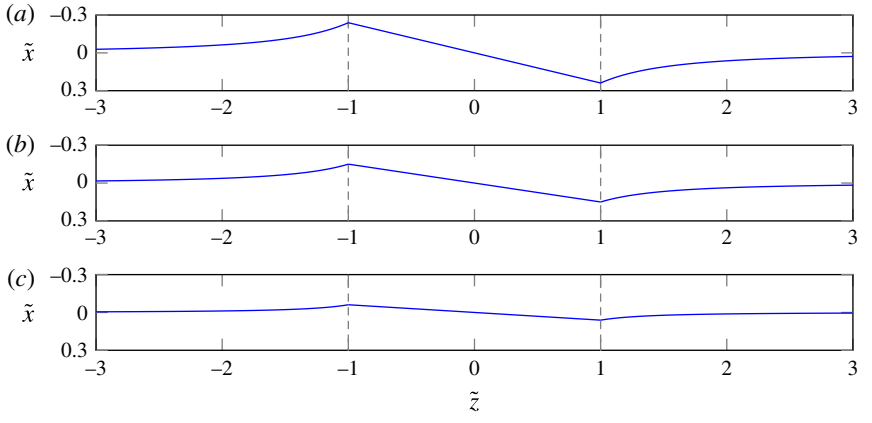


FIGURE 7. (Colour online) Cross-section of the interfacial shape $\tilde{h} = \tilde{h}^{(1)}Ca$ according to (4.18) and of the corresponding TCL for three different equilibrium contact angles Θ and a capillary number of $Ca = 0.3$: (*a*) $\Theta = 75°$, (*b*) $\Theta = 90°$, (*c*) $\Theta = 105°$. The inclination of the TCL is given by the particle trim angle $\alpha = \alpha^{(1)}Ca$ from (4.17); the particle is moving in the $\tilde{z}$-direction.

5. Pair interaction via linear superposition approximation

Within the LSA, the interfacial deformation (4.18) around a single particle is used to construct the two-particle deformation necessary for studying capillary interactions via linear superposition. Since the method can only be expected to be accurate at large inter-particle separation $d \ll a$, we truncate the infinite series in (4.18) after the first, asymptotically dominant, $\tilde{\varrho}^{-2}$-term. Returning to dimensional quantities, but keeping the capillary number as an abbreviation, we may express the deformation h_{pi} around a single particle pi in the form

$$h_{pi} \approx -\tau_1^{(0)} Ca_{pi} \frac{a^3}{3\varrho_i^2} \cos\vartheta_i = Ca_{pi} \left(\frac{1}{2} + \frac{11}{8}\varepsilon\right) \frac{a^3}{\varrho_i^2} \cos\vartheta_i, \quad i = 1, 2. \tag{5.1}$$

https://doi.org/10.1017/jfm.2015.129 Published online by Cambridge University Press

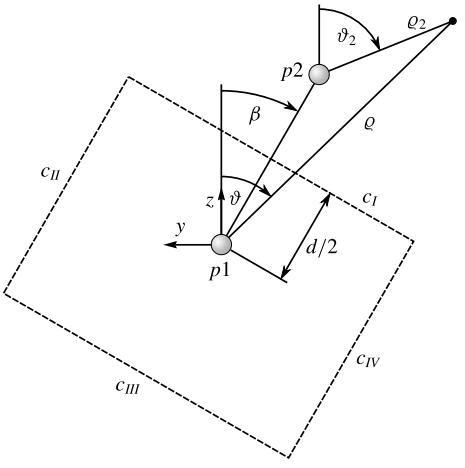


FIGURE 8. Coordinate systems for two interacting particles $p1$ and $p2$ of separation d viewed from the negative x/χ-direction; integration path $c = c_I \cup c_{II} \cup c_{III} \cup c_{IV}$ used in the evaluation of the capillary force.

In (5.1), the cylindrical coordinate system $(\varrho_i, \vartheta_i, \chi)$ is centred at particle i. Since we will later use only the coordinate system of particle 1, we set $(\varrho_1, \vartheta_1, \chi) = (\varrho, \vartheta, \chi)$ for simplicity (see figure 8). The notation Ca_{pi} instead of Ca accounts for a potentially different velocity between the particles (in magnitude and sign). This may apply to the case when the particles differ in the properties governing their reaction to the external field driving them. Figure 8 shows the two particles with their centres separated by a distance $d \gg a$ and with the line connecting their centres coinciding with the coordinate line $\vartheta = \beta$. In the course of the LSA, it is required to re-express the single-particle deformation h_{p2}, which is given by (5.1) within the $(\varrho_2, \vartheta_2, \chi)$-system, in terms of the coordinates $(\varrho, \vartheta, \chi)$. From figure 8, we can geometrically derive the relations

$$\varrho_2 = \sqrt{\varrho^2 + d^2 - 2\varrho d\cos(\vartheta - \beta)}, \quad \text{and} \quad \cos\vartheta_2 = \frac{\varrho\cos\vartheta - d\cos\beta}{\varrho_2}, \tag{5.2a,b}$$

so that we have

$$h_{p2} \approx a^3 \left(\frac{1}{2} + \frac{11}{8}\varepsilon\right) Ca_{p2} \frac{\varrho\cos\vartheta - \mathrm{d}\cos\beta}{\left[\varrho^2 + d^2 - 2\varrho d\cos(\vartheta - \beta)\right]^{3/2}}. \tag{5.3}$$

Regarding the interfacial deformation h_{LSA} in the presence of two particles, the LSA is based on the assumption that

$$h_{LSA} = h_{p1} + h_{p2}. \tag{5.4}$$

Physically, the dynamical deformation of the interface by the particles gives rise to an interaction force. In the present case of two moving particles, the interaction force is expected to be dependent on both the relative positions of the particles (described by β), their separation, and the respective capillary numbers Ca_{pi}. To be sure, the boundary conditions on the particle surfaces are generally not fulfilled by the sum of the deformations according to (5.4). However, in the region halfway between the

https://doi.org/10.1017/jfm.2015.129 Published online by Cambridge University Press

particles, the approximation is supposed to be accurate when the separation d is large. Therefore, a reasonable path of integration ($c = c_I \cup c_{II} \cup c_{III} \cup c_{IV}$, see figure 8) for the interfacial tension force runs through that region and is closed at infinite distance from the particles. The interaction force $\boldsymbol{F}_{int}$ may be written as

$$\boldsymbol{F}_{int} = \oint_c \sigma_{12} \left(\frac{\partial \boldsymbol{r}_c}{\partial s} \times \boldsymbol{n}_{12} \right) \mathrm{d}s, \tag{5.5}$$

where the parametrization of a point $\boldsymbol{r}_c$ on the integration path c based on s is chosen such that the integrand becomes a vector pointing away from particle 1. Prior to its evaluation, the integral in (5.5) can be simplified considerably with the aid of figure 8. First, we understand that the contributions along the paths c_{II} and c_{IV} mutually cancel because the interfacial deformation vanishes at infinite distance from the particles. We are left with the integrals along c_I and c_{III}, which diverge when evaluated separately since the interfacial tension force (more specifically, its line density) becomes constant at infinity. Therefore, both integrals need to be evaluated simultaneously. In effect, the contribution from c_{III} can be taken into account by subtraction of a vector of constant orientation under the integral since, again, the interfacial force is constant at infinity. Choosing $\mathrm{d}s = \mathrm{d}\vartheta$, the vector $\boldsymbol{r}_c$ describing a point on the integration path is given by

$$\boldsymbol{r}_c = \frac{d}{2\cos(\vartheta - \beta)} \boldsymbol{e}_\varrho + h_{LSA}|_{\varrho = d/[2\cos(\vartheta-\beta)]} \, \boldsymbol{e}_\chi, \tag{5.6}$$

with h_{LSA} according to (5.4). The normal vector, which is to be evaluated at $\boldsymbol{r}_c$ using h_{LSA}, is calculated from (4.4). As discussed above, we need to subtract a vector

$$\sigma_{12} \frac{\partial}{\partial \vartheta} \left(\frac{d}{2\cos(\vartheta - \beta)} \boldsymbol{e}_\varrho \right) \times \boldsymbol{e}_\chi \tag{5.7}$$

representing the contribution from c_{III}. Note that with the parametrization $\mathrm{d}s = \mathrm{d}\vartheta$ the vector (5.7) is not constant as it would have been if $\mathrm{d}s$ had been set equal to $\mathrm{d}y$, say. The foregoing expressions are valid for any choice of Ca_{p1} and Ca_{p2}. Within the following discussion, however, we focus on the most relevant case of two particles having identical velocity vectors $U\boldsymbol{e}_z$ and thus set $Ca = Ca_{p1} = Ca_{p2}$. As the evaluation of (5.5) and of the analogous relation for the torque $\boldsymbol{M}_{int}$ with respect to the centre of particle 1 are straightforward from the above considerations, we may directly state the results

$$\frac{\boldsymbol{F}_{int}}{\sigma_{12} a} = -16H \frac{a^2}{d^2} \cos\beta \boldsymbol{e}_x + 3\pi H^2 \frac{a^5}{d^5} \left\{ [4 + 13\cos(2\beta)] \sin\beta \boldsymbol{e}_y + 26 \cos\beta \sin^2\beta \boldsymbol{e}_z \right\}, \tag{5.8}$$

$$\frac{\boldsymbol{M}_{int}}{\sigma_{12} a^2} = -\frac{51}{4} \pi H^2 \frac{a^4}{d^4} \sin(2\beta) \boldsymbol{e}_x - 4H \frac{a}{d} \left[2\cos^2\beta \boldsymbol{e}_y + \sin(2\beta) \boldsymbol{e}_z \right] \tag{5.9}$$

in (x, y, z)-coordinates, where $H := (1/2 + 11\varepsilon/8)Ca$. Recall that the particle motion due to the external force is aligned with the z direction. The first term $\sim d^{-2}$ in (5.8) only results in vertical (x-)adjustment of the particle positions. On the other hand, the remaining two terms $\sim d^{-5}$ act in the plane of the undisturbed fluid interface. In figure 9 the force components are shown qualitatively in the form of a vector pinned at a position determined by the respective value of β. The interaction map may be read as follows. For a given β, the connecting line between the particles $p1$ and $p2$

https://doi.org/10.1017/jfm.2015.129 Published online by Cambridge University Press

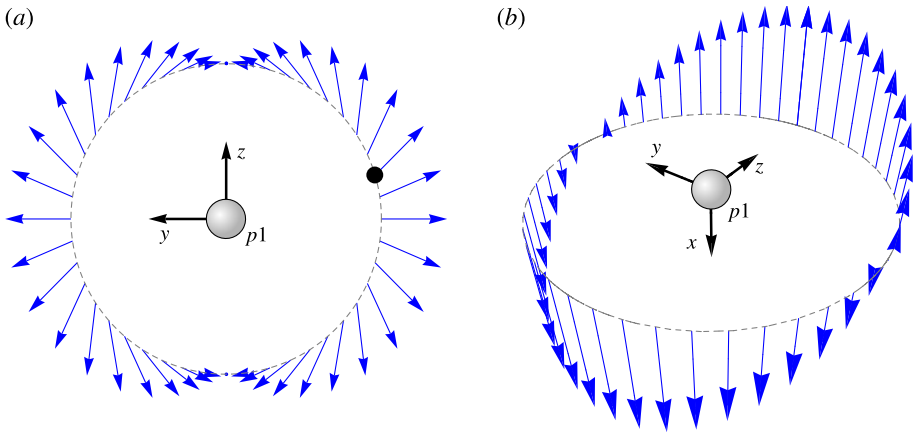


FIGURE 9. (Colour online) Interaction map qualitatively describing the components of the interaction force (5.8) acting on particle 1 dependent on the relative particle positions: (*a*) *y*- and *z*-components, (*b*) *x*-component. The correspondence between length of the vectors and the force magnitude differs between the subfigures.

intersects the dashed circle in figure 9. The vector plotted at the intersection point represents the force acting on particle 1 within the actual configuration. Figure 9(*a*) displays the *y*- and *z*-components of the interaction force while figure 9(*b*) shows its *x*-component. The scaling of the forces differs between figures 9(*a*) and 9(*b*) for reasons of optimal visualization, owing to the different dependences of the force components on the separation d (see (5.8)). In addition to the direction and the relative strength of the forces depending on the particle configuration, figure 9 also contains information on the torque resulting from the interaction. It can be shown that the forces sketched in the figure as pinned to the dashed circle do indeed provide a full representation of the force distribution, meaning that the vector between the centre of particle $p1$ and the respective intersection point on the dashed circle, namely

$$-\tfrac{1}{2}d\sin\beta\boldsymbol{e}_y+\tfrac{1}{2}d\cos\beta\boldsymbol{e}_z \tag{5.10}$$

(see figure 8), equals the lever arm for the calculation of the torque on the particle by means of the interaction force. In other words, we have the relation

$$\boldsymbol{M}_{int}=(-\tfrac{1}{2}d\sin\beta\boldsymbol{e}_y+\tfrac{1}{2}d\cos\beta\boldsymbol{e}_z)\times\boldsymbol{F}_{int}, \tag{5.11}$$

which can be easily verified via (5.8) and (5.9). As an example, consider the black dot in figure 9 symbolizing an intersection point. The force on particle 1 can be read off as pointing to the northeast of the picture while the resulting torque tends to rotate the particle in the anticlockwise direction because the line of action of the force does not run through the particle centre but passes south of it.

From (5.8) and, accordingly, figure 9 it can be seen that the interaction force vanishes when the particles move along a common line. When the second particle's position is on the *y*-axis, the force is attractive and acts along the line of centres. Between those extreme cases the interaction force changes continuously. The force component $F_\parallel$ along the line of centres

$$F_\parallel:=\boldsymbol{F}_{int}\cdot(-\sin\beta\boldsymbol{e}_y+\cos\beta\boldsymbol{e}_z)=\frac{27\pi}{2d^5}H^2\,[1-\cos(2\beta)]\geqslant 0 \tag{5.12}$$

https://doi.org/10.1017/jfm.2015.129 Published online by Cambridge University Press

is generally attractive. Following the commonly accepted method of analysing interfacial deformation by means of a multipole expansion (Danov *et al.* (2005, equation 2.16); Oettel & Dietrich 2008), we identify the interfacial shape (4.18) as dipolar. As a consequence, the interaction between particles driven by an external force, given by (5.8), may also be termed dipolar. In fact, the interaction force between two fixed electric dipoles with equal dipole moments lying within a common plane has the form (Israelachvili 2011, table 2.2, setting $\theta_1 = \theta_2 = \pi/2 - \beta$ and $\phi = 0$)

$$F_{\parallel,el} \sim -1 + 3\cos(2\beta) \tag{5.13}$$

showing the same variation with β as in the case of driven particles.

Since the particles move along the fluid–fluid interface and their motion causes fluid flow, the discussion of interactions between the particles is only complete if we comment on hydrodynamic interactions. For two equal spheres at low Reynolds number in an unbounded fluid acted upon by the same force, it is well known that the particle velocity vectors are always parallel (Russel *et al.* 1989, p. 52; Happel & Brenner 1983, pp. 242–243). In that context, the particles' direction of motion need not be parallel to the driving force vector and the inter-particle separation remains constant during the motion. In the case of particles moving along a fluid–fluid interface considered in the present work, we have already seen that the hydrodynamic problem at zero capillary number can be treated by means of an equivalent problem of a particle in an unbounded fluid (cf. figure 2). Therefore, the aspect of hydrodynamic interactions for the $O(Ca^0)$-problem is also equivalent to the interaction of particles in an unbounded fluid. The same reasoning has been followed by Vassileva *et al.* (2005). As a consequence, the hydrodynamic interaction between particles moving along a fluid interface by action of the same external driving force does not influence their separation, that is, the hydrodynamic force vectors acting on each particle are equal. We conclude that capillary effects govern the interaction between driven interfacial particles at least up to order Ca.

In order to estimate the strength of the dipolar interaction force, varying as d^{-5} according to (5.8), a comparison with another capillary interaction force is instructive, namely the quadrupolar force arising from an undulated TCL (Stamou *et al.* 2000; Danov *et al.* 2005; Domínguez *et al.* 2008). The latter also decays as d^{-5}. Using the values given by Stamou *et al.* (2000) in their estimation, we arrive at the quadrupolar interaction force $F_{\pm} = 48\pi\sigma_{12}a^{-1}\delta x\,\tilde{d}^{-5}$. Thereby, δx is a characteristic undulation of the TCL. Park & Furst (2011) report a value of $\delta x/a = 0.03$ for the particles investigated, leading to $F_{\pm} \approx 0.14\,\sigma_{12}a\tilde{d}^{-5}$. On the other hand, the parallel component of the dipolar interaction force in the case $\varepsilon = 0$ and $\beta = \pi/2$ is $F_{\parallel} \approx 21.21\sigma_{12}aCa^2\tilde{d}^{-5}$. Therefore, the two forces are equal at a capillary number of $Ca \approx 0.08$ corresponding to a particle velocity of $U \approx 1.7$ mm s^{-1} for the 1000 cSt silicone oil used by Ally & Amirfazli (2010). If, of course, the TCL is less irregular, the dipolar force may dominate at an even smaller velocity. The same obviously holds for a liquid of higher viscosity.

6. Conclusions

In this work, we have studied the problem of spherical particles driven along a fluid–fluid interface by an external force. By simultaneously using two asymptotic expansions, we have succeeded in calculating the flow field for equilibrium contact angles not too far away from 90° and the resulting fluid–fluid interfacial deformation.

https://doi.org/10.1017/jfm.2015.129 Published online by Cambridge University Press

The TCL at the surface of the particle has been assumed to be pinned, implying a variation in the contact angle along the surface. At the same time, the particle's response to the torque resulting from the asymmetric drag associated with the difference in fluid viscosity across the fluid–fluid interface has been described. More specifically, the particle rotates by a certain angle which we have termed the trim angle. Knowing the interfacial deformation around a single particle, we have described the capillary interaction between two particles through the linear superposition approximation. The interaction force has been shown to be dipolar in terms of the azimuthal angle and to decay with the fifth power of the separation, similar to a capillary quadrupole arising from undulations of the contact line. To visualize the interaction force vector for varying configurations of the particles, we have introduced an interaction map from which the torque acting on a particle along with the interaction force can be deduced. Hydrodynamic interactions have been discussed and shown to be negligible. The strength of the dipolar interaction has been compared to interactions resulting from undulated contact lines, showing that for particles moving sufficiently fast, the dipolar interaction is dominant.

The reasoning followed in the present work can be applied to particles of more general shapes than spheres, provided that the undeformed, equilibrium fluid–fluid interface is planar, which allows for the construction of an equivalent flow problem by reflection (as shown in figure 2). On the methodological side, corrections to the asymptotic formalism developed by Brenner (1964) are required, as has been demonstrated in § 3. Furthermore, our analysis can easily be extended to incorporate a Navier slip condition on the particle surface, which may become relevant for nanoparticles.

As discussed above, the particle motion is associated with a configurational change parametrized by the trim angle. When the corresponding change in contact angle exceeds the range of contact angles permitted by contact angle hysteresis, we expect a qualitative change of the situation. For instance, the particle may detach from the interface and cause anomalous diffusional behaviour as reported by Chen & Tong (2008) and Sriram *et al.* (2012).

The above analysis is based on the assumption of small Reynolds numbers leading, in particular, to a flow field with a fore-and-aft symmetry. Consequently, we have found an interfacial shape displaying the same type of symmetry. For finite Reynolds numbers, however, the interfacial shape becomes asymmetric and evolves into a fascinating wave pattern (Moisy & Rabaud 2014) implying additional wave-making resistance. A possible route to the analytical treatment of the problem, which is left for future research, could rely on the Oseen approximation.

REFERENCES

ALLY, J. & AMIRFAZLI, A. 2010 Magnetophoretic measurement of the drag force on partially immersed microparticles at air–liquid interfaces. *Colloids Surf.* A **360**, 120–128.

BERDAN, C. II & LEAL, L. G. 1982 Motion of a sphere in the presence of a deformable interface. Part I. Perturbation of the interface from flat: the effects on drag and torque. *J. Colloid Interface Sci.* **87** (1), 62–80.

BINKS, B. P. 2002 Particles as surfactants: similarities and differences. *Curr. Opin. Colloid Interface Sci.* **7**, 21–41.

BŁAWZDZIEWICZ, J., EKIEL-JEŻEWSKA, M. L. & WAJNRYB, E. 2010 Motion of a spherical particle near a planar fluid–fluid interface: the effect of surface incompressibility. *J. Chem. Phys.* **133**, 114702.

https://doi.org/10.1017/jfm.2015.129 Published online by Cambridge University Press

BRENNER, H. 1964 The Stokes resistance of a slightly deformed sphere. *Chem. Engng Sci.* **19**, 519–539.

BYERLY, W. E. 1893 *An Elementary Treatise on Fourier's Series and Spherical, Cylindrical, and Ellipsoidal Harmonics*. Ginn & Company.

CHAN, D. Y. C., HENRY, J. D. JR & WHITE, L. R. 1981 The interaction of colloidal particles collected at fluid interfaces. *J. Colloid Interface Sci.* **79** (2), 410–418.

CHEN, W. & TONG, P. 2008 Short-time self-diffusion of weakly charged silica spheres at aqueous interfaces. *Eur. Phys. Lett.* **84**, 28003.

CICHOCKI, B., EKIEL-JEŻEWSKA, M. L., NÄGELE, G. & WAJNRYB, E. 2004 Motion of spheres along a fluid–gas interface. *J. Chem. Phys.* **121**, 2305–2316.

DANOV, K., AUST, R., DURST, F. & LANGE, U. 1995 Influence of the surface viscosity on the hydrodynamic resistance and surface diffusivity of a large Brownian particle. *J. Colloid Interface Sci.* **175**, 36–45.

DANOV, K. D., GURKOV, T. D., RASZILLIER, H. & DURST, F. 1998 Stokes flow caused by the motion of a rigid sphere close to a viscous interface. *Chem. Engng Sci.* **53** (19), 3413–3434.

DANOV, K. D., KRALCHEVSKY, P. A., NAYDENOV, B. N. & BRENN, G. 2005 Interactions between particles with an undulated contact line at a fluid interface: capillary multipoles of arbitrary order. *J. Colloid Interface Sci.* **287**, 121–134.

DASSIOS, G. & VAFEAS, P. 2001 Connection formulae for differential representations in Stokes flow. *J. Comput. Appl. Maths* **133**, 283–294.

DOMÍNGUEZ, A., OETTEL, M. & DIETRICH, S. 2008 Force balance of particles trapped at fluid interfaces. *J. Chem. Phys.* **128**, 114904.

DU, K., LIDDLE, J. A. & BERGLUND, A. J. 2012 Three-dimensional real-time tracking of nanoparticles at an oil–water interface. *Langmuir* **28**, 9181–9188.

FISCHER, T. M., DHAR, P. & HEINIG, P. 2006 The viscous drag of spheres and filaments moving in membranes or monolayers. *J. Fluid Mech.* **558**, 451–475.

FORTES, M. A. 1982 Attraction and repulsion of floating particles. *Can. J. Chem.* **60**, 2889–2895.

FULFORD, G. R. & BLAKE, J. R. 1986 Force distribution along a slender body straddling an interface. *J. Austral. Math. Soc.* B **27**, 295–315.

GHEZZI, F., EARNSHAW, J. C., FINNIS, M. & MCCLUNEY, M. 2001 Pattern formation in colloidal monolayers at the air–water interface. *J. Colloid Interface Sci.* **238**, 433–446.

HAPPEL, J. & BRENNER, H. 1983 *Low Reynolds Number Hydrodynamics*. Martinus Nijhoff.

HOROZOV, T. S., AVEYARD, R. & CLINT, J. H. 2005 Particle zips: vertical emulsion films with particle monolayers at their surfaces. *Langmuir* **21**, 2330–2341.

HUH, C. & MASON, S. G. 1974 The flotation of axisymmetric particles at horizontal liquid interfaces. *J. Colloid Interface Sci.* **47** (2), 271–289.

ISRAELACHVILI, J. N. 2011 *Intermolecular and Surface Forces*, 3rd edn. Academic.

KOSER, A. E., KEIM, N. C. & ARRATIA, P. E. 2013 Structure and dynamics of self-assembling colloidal monolayers in oscillating magnetic fields. *Phys. Rev.* E **88**, 062304.

KRALCHEVSKY, P. A. & NAGAYAMA, K. 2000 Capillary interactions between particles bound to interfaces, liquid films and biomembranes. *Adv. Colloid Interface Sci.* **85**, 145–192.

LAMB, H. 1932 *Hydrodynamics*, 6th edn. Cambridge University Press.

LEE, S. H., CHADWICK, R. S. & LEAL, L. G. 1979 Motion of a sphere in the presence of a plane interface. Part 1. An approximate solution by generalization of the method of Lorentz. *J. Fluid Mech.* **93** (4), 705–726.

MOISY, F. & RABAUD, M. 2014 Mach-like capillary–gravity wakes. *Phys. Rev.* E **90**, 023009.

NICOLSON, M. M. 1949 The interaction between floating particles. *Math. Proc. Camb. Phil. Soc.* **45** (2), 288–295.

OETTEL, M. & DIETRICH, S. 2008 Colloidal interactions at fluid interfaces. *Langmuir* **24**, 1425–1441.

OETTEL, M., DOMÍNGUEZ, A. & DIETRICH, S. 2005 Effective capillary interaction of spherical particles at fluid interfaces. *Phys. Rev.* E **71**, 051401.

O'NEILL, M. E., RANGER, K. B. & BRENNER, H. 1986 Slip at the surface of a translating–rotating sphere bisected by a free surface bounding a semi-infinite viscous fluid: removal of the contact-line singularity. *Phys. Fluids* **29**, 913–924.

https://doi.org/10.1017/jfm.2015.129 Published online by Cambridge University Press

PARK, B. J. & FURST, E. M. 2011 Attractive interactions between colloids at the oil–water interface. *Soft Matt.* **7**, 7676–7682.

PETKOV, J. T., DENKOV, N. D., DANOV, K. D., VELEV, O. D., AUST, R. & DURST, F. 1995 Measurement of the drag coefficient of spherical particles attached to fluid interfaces. *J. Colloid Interface Sci.* **172**, 147–154.

PITOIS, O. & CHATEAU, X. 2002 Small particle at a fluid interface: effect of contact angle hysteresis on force and work of detachment. *Langmuir* **18**, 9751–9756.

POZRIKIDIS, C. 2007 Particle motion near and inside an interface. *J. Fluid Mech.* **575**, 333–357.

RADOEV, B., NEDJALKOV, M. & DJAKOVICH, V. 1992 Brownian motion at liquid–gas interfaces. Part 1. Diffusion coefficients of macroparticles at pure interfaces. *Langmuir* **8**, 2962–2965.

RAWSON, K. J. 2001 *Basic Ship Theory*, vol. 1. Butterworth-Heinemann.

RUSSEL, W. B., SAVILLE, D. A. & SCHOWALTER, W. R. 1989 *Colloidal Dispersions*. Cambridge University Press.

SINGH, P. & HESLA, T. I. 2004 The interfacial torque on a partially submerged sphere. *J. Colloid Interface Sci.* **280**, 542–543.

SINGH, P. & JOSEPH, D. D. 2005 Fluid dynamics of floating particles. *J. Fluid Mech.* **530**, 31–80.

SINGH, P., JOSEPH, D. D., FISCHER, I. S. & DALAL, B. 2011 Role of particle inertia in adsorption at fluid–liquid interfaces. *Phys. Rev.* E **83**, 041606.

SRIRAM, I., WALDER, R. & SCHWARTZ, D. K. 2012 Stokes–Einstein and desorption-mediated diffusion of protein molecules at the oil–water interface. *Soft Matt.* **8**, 6000–6003.

STAMOU, D., DUSCHL, C. & JOHANNSMANN, D. 2000 Long-range attraction between colloidal spheres at the air–water interface: the consequence of an irregular meniscus. *Phys. Rev.* E **62** (4), 5263–5271.

VASSILEVA, N. D., VAN DEN ENDE, D., MUGELE, F. & MELLEMA, J. 2005 Capillary forces between spherical particles floating at a liquid–liquid interface. *Langmuir* **21**, 11190–11200.

WÜRGER, A. 2014 Thermally driven Marangoni surfers. *J. Fluid Mech.* **752**, 589–601.

ZABARANKIN, M. 2007 Asymmetric three-dimensional Stokes flow about two fused equal spheres. *Proc. R. Soc. Lond.* A **463**, 2329–2349.

https://doi.org/10.1017/jfm.2015.129 Published online by Cambridge University Press